ORIGINAL ARTICLE

Inorganic–organic nanohybrid of MoS$_2$-PANI for advanced photocatalytic application

Shreya Saha[1] · Nahid Chaudhary[1] · Honey Mittal[1] · Govind Gupta[2] · Manika Khanuja[1]

Abstract

In this work, the fabrication of MoS$_2$-Polyaniline (PANI) nanocomposites, by in situ polymerization, has been described and its application as a photocatalyst for the degradation of organic pollutants such as methylene blue (MB) and 4-chlorophenol (4-CP), has been reported. The disadvantages of MoS$_2$ such as poor electronic conductivity and agglomeration between the nanosheets, was overcome by intercalating 2D MoS$_2$ layers with 1D conducting polymer, Polyaniline (PANI). The composite material was characterised by SEM, TEM, BET, XRD, FTIR, UV–Vis spectroscopy and XPS, indicating proper intercalation between MoS$_2$ nanosheets and PANI. Consequently, the synthesized composites were used for the degradation of MB and 4-CP, followed by kinetic investigations to determine the rate kinetics. The photoactivity of the nanocomposite is explained by the transfer of photogenerated electrons from PANI to the CB of MoS$_2$, thus preventing the direct recombination of electrons and holes. Hence, a positive synergistic effect between MoS$_2$ and PANI resulted in efficient photocatalytic degradation of organic dyes like MB.

Keywords Hydrothermal · MoS$_2$-PANI hybrid · Photocatalysis · Pseudo first order rate kinetics

Introduction

In search of highly efficient photocatalytic materials, 2D nanostructures have attracted tremendous interest as a possible replacement of existing photocatalytic materials due to their visible light driven photocatalytic activity. Two dimensional (2D) metal dichalcogenide (MoS$_2$), is known for its remarkable photocatalytic properties arising from its unique physicochemical characteristics such as porous structure, large surface areas and active sites, good crystallinity and better separation of charge carriers, etc [1–3]. Despite all its advantages, poor electronic conductivity acts as a major drawback in employing MoS$_2$ as a photocatalytic material [4]. Also, the weak interlayer bonding and large interlayer spacing causes stacking of MoS$_2$ nanosheets [5, 6]. Several attempts have been made in the direction to improve

conductivity of MoS$_2$ and prevent its aggregation with carbon nanotubes and stacking with graphene [7, 8]. However, there has been limited improvement due to relative decline in number of interconnected conductive pathways. The use of numerous existing metal oxides, e.g., WO$_3$, TiO$_2$, ZnO, and SnO$_2$ as photocatalyst, is also restricted due to: (1) wide band gap which hinders the complete use of sunlight for charge carrier generation, (2) low mobility which prevents charge transport, (3) diminishing photocatalytic activity due to rapid recombination of photogenerated electron–hole pairs, and (4) agglomeration of nanomaterials leading to poor dispersion [9, 10]. In view of the above, the work presented here reports a simple synthesis of 3D architectures composed of two-dimensional MoS$_2$ nanosheets and one-dimensional conducting polymer polyaniline (PANI) as an effective approach to solve the aforementioned issues.

Polyaniline offers an extended p-conjugated electron system and remarkable properties viz. visible region absorption and generation of highly mobile charge carriers [11, 12]. It has found extensive use in solar energy and photocatalytic activity owing to its reasonable cost, excellent environmental stability and facile synthesis methods [13, 14]. PANI is treated equivalent to p-type inorganic semiconductors due to its high hole concentration. Integration of MoS$_2$

✉ Manika Khanuja
manikakhanuja@gmail.com

1 Center for Nanoscience and Nanotechnology, Jamia Millia Islamia, New Delhi 110125, India

2 Advanced Materials and Devices Division, CSIR-National Physical Laboratory (NPL), Dr. K.S. Krishnan Road, New Delhi 110012, India

nanosheets with PANI improves the electrical conductivity of the nanosheets, reduces the electron hole recombination probability, prevents MoS$_2$ from agglomeration, leading to enhancement in surface area [14]. It is, therefore, believed that the proposed hybrid, MoS$_2$-PANI nanostructure, will have the potential to overcome the challenges prevalent in existing photocatalytic materials and also provide an optimum solution for the elimination of dyes and pollutants from waste water for water purification.

Herein, MoS$_2$-PANI hybrid is used as a catalyst for the photodegradation of 4-chlorophenol (4-CP) and methylene blue (MB). MB is an organic photoactive dye which is used for biological applications. However, MB is hazardous to living beings as it can cause ailments such as tissue necrosis, diarrhoea, cyanosis and jaundice while 4-CP is a major toxic chemical pollutant which causes severe health issues including histopathological alterations, genotoxicity, mutagenicity and carcinogenicity [13, 14]. The removal of these pollutants is therefore crucial in restoring water quality. A study of the intermediates that were formed during degradation of 4-CP were also processed using high performance liquid chromatography (HPLC).

Experimental details

Materials and reagents

Synthesis of MoS$_2$: sodium molybdate (Na$_2$MoO$_4$·2H$_2$O, Thermo Fisher Scientific India Pvt. Ltd), thioacetamide (C$_2$H$_5$NS, Central Drug House Pvt. Ltd.) and silicotungstic acid AR(H[Si(W$_3$O$_{10}$)$_4$]. XH$_2$O with max impurity limit of 0.009%, Central Drug House Pvt. Ltd.).

Synthesis of PANI: aniline (C$_6$H$_5$NH$_2$ with max impurity limit of 0.02%, Central Drug House Pvt. Ltd.), hydrochloric acid (HCl.H$_2$O with max impurity limit of 0.0316%, Thermo Fisher Scientific India Pvt. Ltd.) and ammonium persulphate [(NH$_4$)$_2$S$_2$O$_8$ with max impurity limit of 0.005%, Sisco Research Laboratories Pvt. Ltd.].

Synthesis of MoS$_2$-PANI

Figure 1 depicts the synthesis procedure for the nanohybrid which was obtained by in situ oxidative polymerization of aniline with MoS$_2$ nanosheets, in the presence of an oxidiser, ammonium persulphate (APS). MoS$_2$ nanosheets were prepared by a hydrothermal method [15]. The first step involved is the synthesis of MoS$_2$ nanosheets by a hydrothermal process (Fig. 1, Scheme I). A suspension was prepared by ultrasonication of 0.1 g of MoS$_2$ nanosheets in 20 mL of DI water. High and low pressure waves generated during ultrasonication cause the formation and subsequent breakage of vacuum bubbles, called cavitation. Thus, high speed liquid

jets and hydrodynamic shear forces cause uniform distribution of agglomerated MoS$_2$ nanosheets in the liquid. In the second step, (Fig. 1, Scheme 2), 1 mL of aniline (100% in concentration), 3 mL of HCl (0.5 M, 25% in concentration) and 16 mL of DI water were added together and refrigerated for 3 h. The suspension of MoS$_2$ nanosheets was added to the above refrigerated solution and kept in an ice bath (-5 °C). Finally, 13 mL of APS (0.1 M in 50 mL) was added to this mixture and continuously stirred for 3 h. After 3 h, ethanol and DI water were used to wash the solution. The black precipitate of MoS$_2$-PANI nanohybrid obtained after filtration, was dried in vacuum at 80 °C for approx. 2 h.

Materials characterization

The morphology and structural properties were examined using a Quanta 3D FEG, (FEI's) Scanning Electron Microscope (SEM) and TECNAI F30 S-Twin High Transmission electron microscopy (HRTEM) working at 300 kV. For TEM analysis, the sample was ultrasonically dispersed in ethanol. Cu-coated TEM grid was then dipped into the sample solution, followed by drying for 24 h. Brunauer–Emmett–Teller (BET) (NOVA-1000 version 370) using N$_2$ as analysis gas, measured at 77.4 K, was used to determine the pore size distribution of the sample. The elemental constituents of the nanocomposite were determined by energy dispersive spectroscopy (EDS) that was integrated into the SEM system. The crystal structure of the nanocomposite was analysed using Rigaku Smart Lab X–ray diffractometer with Cu K$_\alpha$ radiation at 1.540 Å with 2θ varying between 5° and 90°. A Bruker Optik, Vertex 70V spectrometer scanning in the range of 400–4000 cm^{-1} with a step size of 4 cm^{-1} was used for High Resolution Fourier Transform Infrared Spectroscopy (HR-FTIR). UV–Vis spectrophotometer (Agilent technologies, model no: Cary 100 series) was used to determine the band gap of the synthesized material. Elemental identification and the oxidation states of the different elements in the sample were determined by X-Ray Photoelectron Spectroscopy (Multiprobe Surface analysis system, Omicron). The nanocomposite was also characterised by SEM, XRD and FTIR after the photocatalytic reactions.

Photocatalytic experiments

The testing of the photocatalytic efficiency of MoS$_2$-PANI composite was performed using Newport Research Arch Lamp Housing, model no. 66902 (50–500 W) which was connected to an external power supply. A catalyst concentration of 10 mg/100 mL was maintained for all the photocatalytic degradation experiments. A quantity of 0.33 mg MB was dissolved in the solution which was irradiated with UV light (100 W/cm^2) for over 2 h. At time intervals of 15 min, 1 ml aliquots were sampled out

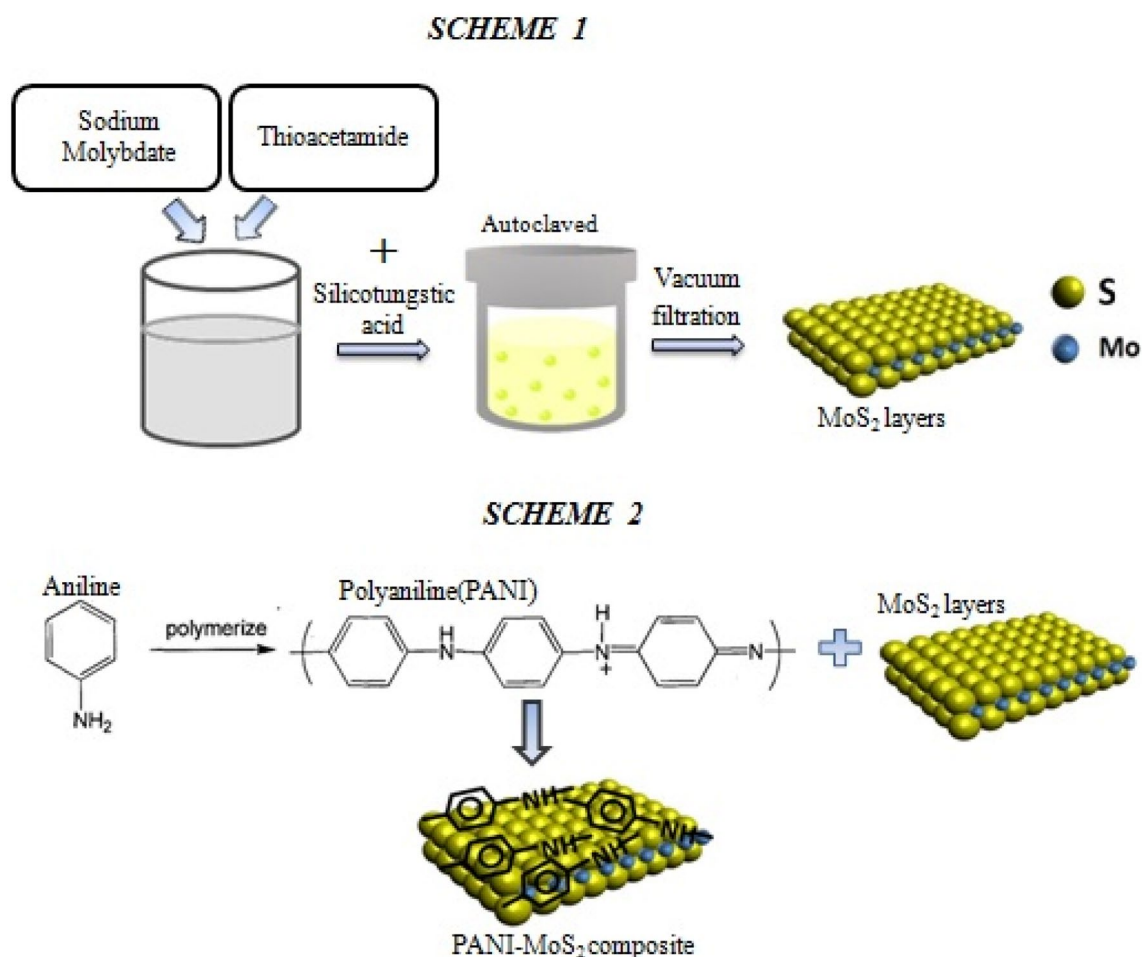## SCHEME 1

SCHEME 2

Fig. 1 Steps involved in the synthesis of MoS₂-PANI composite

and the concentration change of MB was determined by observing the absorption spectra at 664 nm using UV–Vis spectroscopy. Similarly, for the degradation of 4-CP, 50 mg of the catalyst was dissolved in 100 ml solution containing 0.005 g of 4-CP. Characteristic absorption at 225 nm indicated the change in the concentration of 4-CP.

Analysis of intermediates

The intermediates that were formed during the degradation of 4-CP in the presence of MoS₂-PANI, were analysed through HPLC using N2000 Chromatography Data System (Spectra Lab Scientific Inc.) DI water was used as the mobile phase with a flow rate of 0.6 mL/min. The samples were injected at a temperature of 65 °C.

Results and discussion

SEM images of MoS₂-PANI composite are as shown in Fig. 2a, b. Highly dense nanosheets with tubular morphology and inter-fibre fusions are evident. As shown in Fig. 2c, d, TEM images clearly depict the two contrasted regions, dark region representing ultra-thin MoS₂ nanosheets and the lighter region represents tubular PANI nanostructures. The overall structure appeared to be porous. In the MoS₂-PANI hybrid structure, the interlayer spacing is found to be 0.75 nm as evident from HRTEM image (Fig. 2d). SEM and TEM images revealed that the sample has uniform morphology.

Brunauer–Emmett–Teller (BET) analysis confirmed the pore size distribution, surface area and pore volume as shown in Fig. 3 and inset which shows the Barrett–Joyner–Halenda (BJH) plot. According to BET classification, the graph shown matches well with TYPE H4,
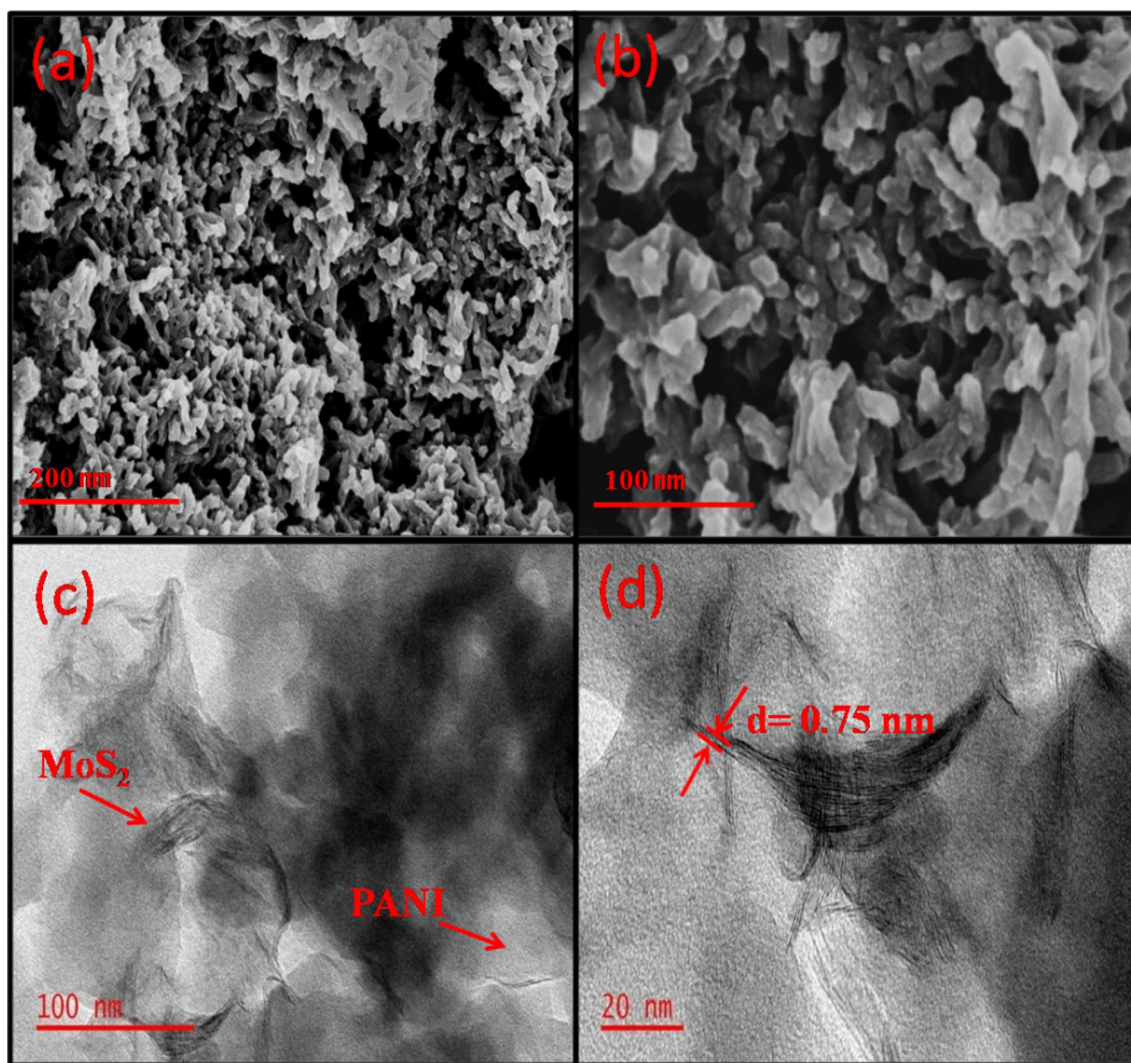
Fig. 2 SEM image of MoS$_2$-PANI at different scales of **a** 200 nm and **b** 100 nm. TEM images of MoS$_2$-PANI at scales of **c** 100 nm and **d** 20 nm

according to standard IUPAC classification, and forms hysteresis loop which is observed for mesoporous structures [16, 17]. The pore diameter and volume are found to be 2.39 nm and 0.071 cc/g, respectively.

EDS analysis and elemental mapping confirmed the chemical composition of MoS$_2$-PANI nanocomposite with the presence of molybdenum (Mo), carbon (C), nitrogen (N), oxygen (O) and sulphur (S), represented by different colours, red, green, blue, cyan, and purple, respectively, as shown in Fig. 4.

Figure 5 shows the X-ray diffractogram of MoS$_2$-PANI nanohybrid. Diffraction peaks were observed at 2θ: 8.45°, 14.83°, 20.90° and 26.31° which correspond to (001), (011), (020) and (200) reflections (marked with black circles) of PANI [18]. The broadening of the peaks indicate an amorphous nature of the polymer [19]. The peaks (marked with

black rectangles) centred at 2θ (hkl): 14.33° (002), 38.23° (103), 44.40° (009), 58.27° (110), 64.76° (01111), 77.77° (0010) and 81.96° (0114) correspond to the hexagonal structure of MoS$_2$ [2, 20]. Therefore, integration of PANI does not change the structural property of MoS$_2$.

The UV–Vis absorbance measurements for MoS$_2$-PANI composite are shown in Fig. 6. The composite showed increased visible light absorption which may be due to the presence of MoS$_2$ and PANI, both of which are visible light driven. MoS$_2$ nanosheets showed characteristic absorption shoulder peaks around 600 and 400 nm [21] while PANI shows characteristic peaks in the range of 280–335 nm [22], and at 638 nm [23]. An absorption maximum at 444.2 nm was observed for MoS$_2$-PANI composite, when irradiated with UV light, which is in agreement with the absorption phenomena shown by both MoS$_2$ and PANI, indicating the
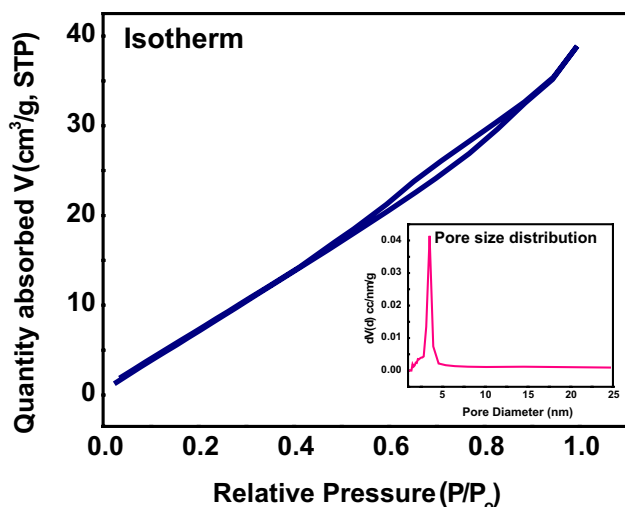
Fig. 3 Adsorption–desorption N_2 isotherm of MoS_2-PANI nanohybrid and Barrett–Joynere–Halenda (BJH) pore size distribution in the inset

formation of inorganic–organic nanohybrid. The estimated band gap of the obtained nanocomposite was determined using Tauc's equation, given as $\alpha h\upsilon = A(h\upsilon - E_g)^n$ where $h\upsilon$ is photon energy, E_g is the optical band gap, α is the absorption coefficient and n = ½ for direct transition mode [24]. The inset of Fig. 4 shows the calculated band gap as 2.73 eV.

The molecular structure MoS_2-PANI nanocomposite was identified using FTIR spectroscopy as shown in Fig. 7. The nanocomposite shows a peak at 809 cm^{-1} which may be assigned to the out of plane C–H in the benzene ring. The peak at 1256 cm^{-1} is attributed to C–N stretching. Peaks at 1540 and 1558 cm^{-1} indicate C=C stretching in the quinone and benzene rings, respectively. The small hump (1118–1135 cm^{-1}) may be assigned to the in-plane C-H vibration. The characteristic peak for Mo-S vibrations which occurs at 480 cm^{-1}, has undergone a shift towards higher wavenumber at 548 cm^{-1} in case of MoS_2-PANI. O–H stretching vibrations in MoS_2 were also observed at 1650 cm^{-1} [4, 20, 25].

XPS is a very powerful technique for elemental identification and evaluation of chemical states [26, 27] and was used to determine the oxidation states of the elements present in the nanocomposite. The general scan of all the elements of the nanohybrid is shown in Fig. 8a while the XPS deconvoluted core level spectra of Mo(3d) and S(2p) elements are shown in Fig. 8b, c. The deconvolution of the spectrum indicates peaks of Mo(3d) at 228.59 eV, assigned to the binding energy of Mo (IV)(3d$_{5/2}$) and 231.91 eV which represents the binding energy of Mo (IV)(3d$_{3/2}$), which are indicative of the presence of Mo-S bonds. The spin orbit doublets of Mo(V) resulting from oxysulfide intermediate phases, occur at 231.47 eV for Mo(V)(3d$_{5/2}$) and 234.71 eV for Mo(V)

(3d$_{3/2}$). The probable formation of MoO_3 indicates higher oxidation states of Mo(VI) present as shoulder peaks. The peak value at 232.19 corresponds to Mo (VI)(3d$_{5/2}$) and the one at 235.41 eV represents Mo (VI)(3d$_{3/2}$). In case of sulphur, two spin–orbit doublets were observed in addition to a small peak at 225.64 eV, complying with the binding energy of the S (2 s) electron. The presence of divalent sulphide ions is indicated by peaks at 160.93 eV and 162.12 eV, representative of the energy of S (2p$_{3/2}$) and S (2p$_{1/2}$) respectively. An extra set of doublets present due to the occurrence of amorphous sulphur is observed at 163.45 eV and 164.82 eV. The deconvoluted spectrum for N (1 s) consists of three peaks positioned at 399.03, 399.75 and 401.05 eV, as shown in Fig. 8d. The first peak is assigned to quinoid diamine nitrogen, the second peak is attributed to benzenoid diamine nitrogen and the third peak at 401.05 eV indicates positively charged nitrogen [28].

Photocatalytic experiments and kinetic analysis

Figure 9 shows the absorbance spectra of MB in the presence of MoS_2-PANI photocatalyst, when irradiated with UV-light for over 2 h. Prior to exposure to UV-light, both the solutions for MoS_2 and MoS_2-PANI were kept in the dark for 45 min. Subsequently, after exposure, there was a gradual decrease in the concentration of dye particles which was indicated by the absorbance of MB at 664 nm. MoS_2-PANI composites exhibited 30% dye degradation in less than 3 h and the photocatalytic efficiency (η), given as $\frac{C - C_0}{C_0} \times 100$ is shown in the inset of Fig. 9.

The photocatalytic degradation profile is shown in Fig. 10a. It is clearly seen from the figure that comparatively high concentration of dye, in the beginning, results in faster degradation which is then followed by a slower adsorption stage.

The adsorption mechanism of MB was analysed by linear pseudo first order and second order models for the investigation of kinetics. To allow slow adsorption process for better kinetic studies, 5 mg MoS_2-PANI sample was used. The pseudo first order model is expressed as

$$Q_t = Q_e\left(1 - e^{-k_1 t}\right)$$

$$where, \quad Q_e = \left(C_0 - C_e\right) \times \frac{V}{W}, \; Q_t = \left(C_0 - C_t\right) \times \frac{V}{W}$$

$$\tag{1}$$

where Q_t (mg g^{-1}) indicates the amount of dye adsorbed at time t (min) and Q_e (mg g^{-1}) represents the amount of dye adsorbed when equilibrium is attained, k_1 (g mg^{-1} min^{-1}) stands for pseudo first order rate constant, C_e (mg L^{-1}) is the equilibrium concentration, C_t is the concentration at time t,
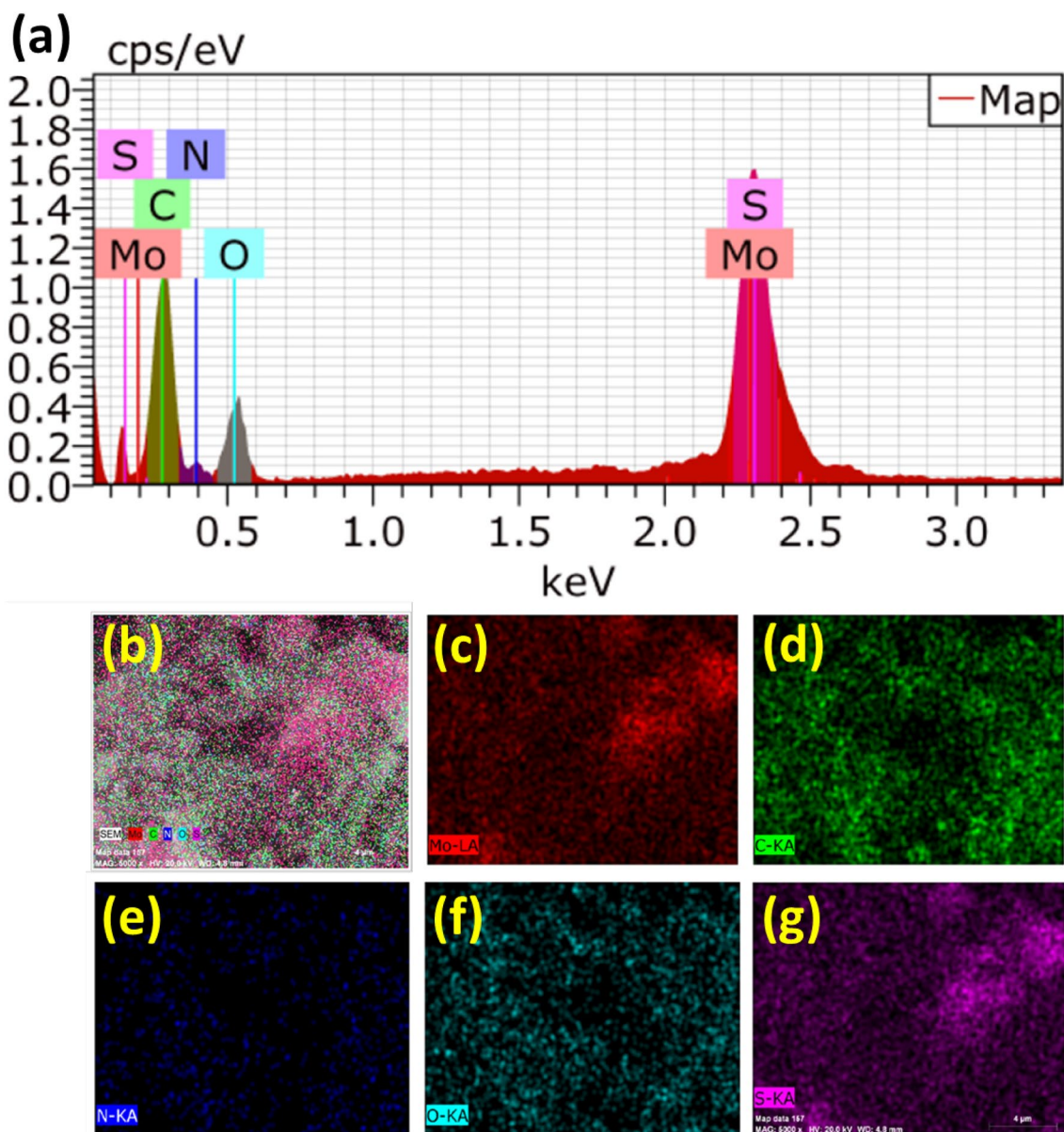
Fig. 4 **a**, **b** EDS images and elemental mapping of MoS$_2$-PANI, **c** Molybdenum (Mo), **d** Carbon (C), **e** Nitrogen (N), **f** Oxygen (O) and **g** Sulphur (S), represented by different colours red, green, blue, cyan and purple, respectively

V(L) represents the volume of the solution and W(g) is the amount of MoS$_2$-PANI used for MB dye adsorption [29, 30].

Pseudo first order represents a process which depends on Van der Waals interaction between the adsorbate (MB) and adsorbent (MoS$_2$-PANI). This is a weak adsorption process involving no chemical interaction between the adsorbate and adsorbent [31]. The fitting results of pseudo first order model are shown in Fig. 10b. First order rate constant (k_1) is found to be 0.0163 g mg^{-1} min^{-1} from the slope of the above graph. Moreover, R^2 (correlation coefficient) value of the plot is found to be 0.9623. High value of R^2 reveals that

adsorption kinetics is following the first order adsorption model.

The second order adsorption equation is given by:

$$\frac{t}{Q_t} = \frac{1}{k_2 Q_e^2} + \frac{t}{Q_e} \qquad (2)$$

where k_2 is the second order rate constant [30].

Figure 10c shows the fitting results of pseudo second order model. Low values of R^2, i.e., 0.1104 indicate that pseudo second order adsorption model is not applicable. Additionally, the theoretical and experimental values of
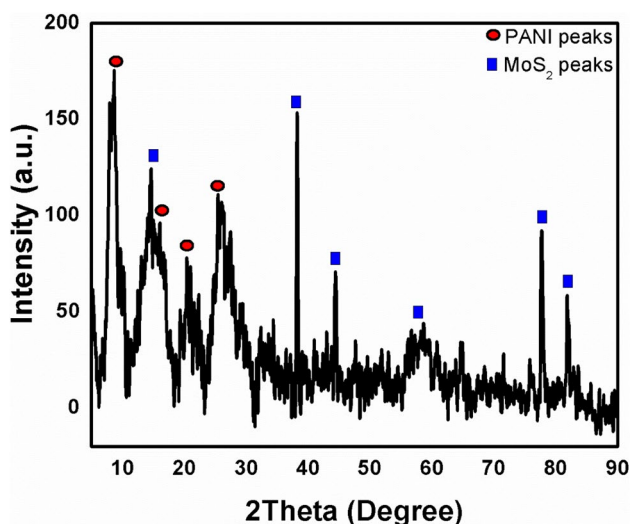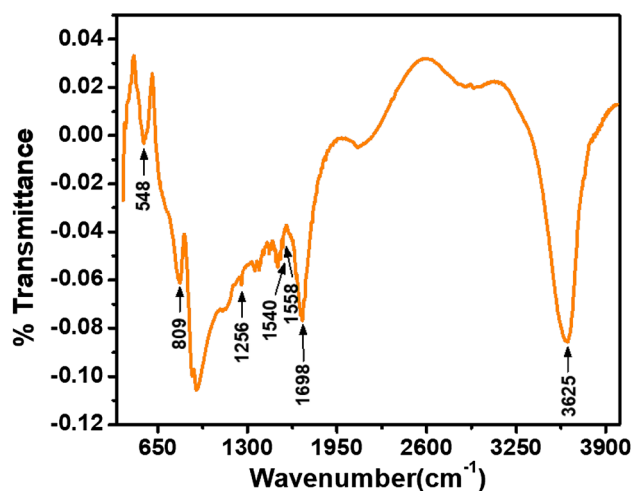
Fig. 5 XRD pattern of MoS$_2$-PANI composite

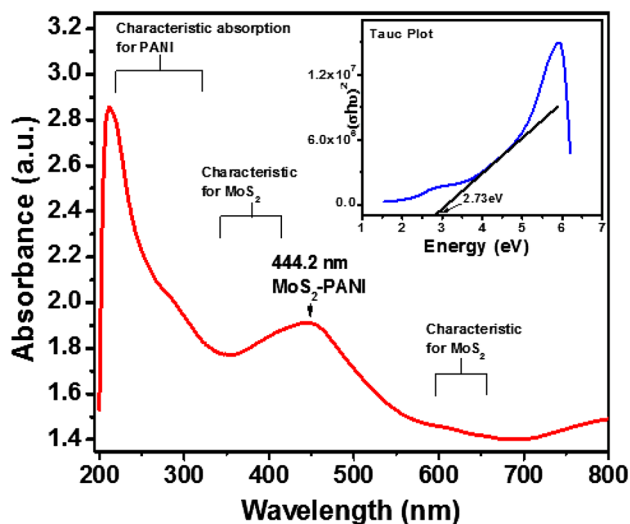**Fig. 7** FTIR spectrum of MoS$_2$-PANI composite

Fig. 6 UV–Vis absorbance spectrum of MoS$_2$-PANI composite (inset shows respective Tauc plot)

Q_e were not found to be in good match which implied that adsorption kinetics cannot be well explained by pseudo second order adsorption model [32]. Pseudo second order model presents the chemisorption process which involves the formation of relatively strong bonds with the surfaces [33].

Other kinetic models such as the diffusion based model were also used to study the adsorption process in heterogeneous systems. In general, adsorption process involves four types of resistances: (1) bulk, (2) film diffusion, (3) intra-particle diffusion, and (4) adsorption processes. Among these, the intra-particle diffusion model involves

pore (crack)/surface diffusion and is given by the following equation:

$$Q_t = k_{id}t^{0.5} + C, \tag{3}$$

where k_{id} is the intra particle diffusion rate constant and C is the intercept representing the boundary layer thickness. Intra-particle diffusion model is the rate determining step in case of a linear plot (from Eq. 3) passing through the origin. A case opposite to the above, indicates different mass transfer rates in the initial and final stages of adsorption, indicating the involvement of film diffusion in addition to intra particle diffusion [33, 34].

Figure 10d shows the linear fitting plot of intra particle diffusion model. The values of correlation coefficients were found to be 0.8733, 0.9960 and 0.7878. The linear fitting of the plot passes through the origin, implying that intra particle diffusion is the rate controlling step in the adsorption process. In the plot, three different intra particle diffusion rate constants are shown. This is explained as (1) for steep slope, adsorption process is fast indicating electrostatic interaction between MB and MoS$_2$ nanosheets, (2) gradual slope indicates diffusion of dye molecules into the MoS$_2$ nanosheets which is a slow process. (3) The flat slope indicates the region where equilibrium is achieved when the diffusion of dye molecules is blocked. The fitting results for all the three models are summarised in Table 1.

The photocatalytic degradation profile of MoS$_2$ for MB degradation is also shown for reference in Fig. 11. The low efficiency of MoS$_2$-PANI compared to MoS$_2$ may be due to blocking of the surface sites of MoS$_2$ by PANI, which maybe unfavourable for the photocatalytic reaction due to lack of available surface area [35].
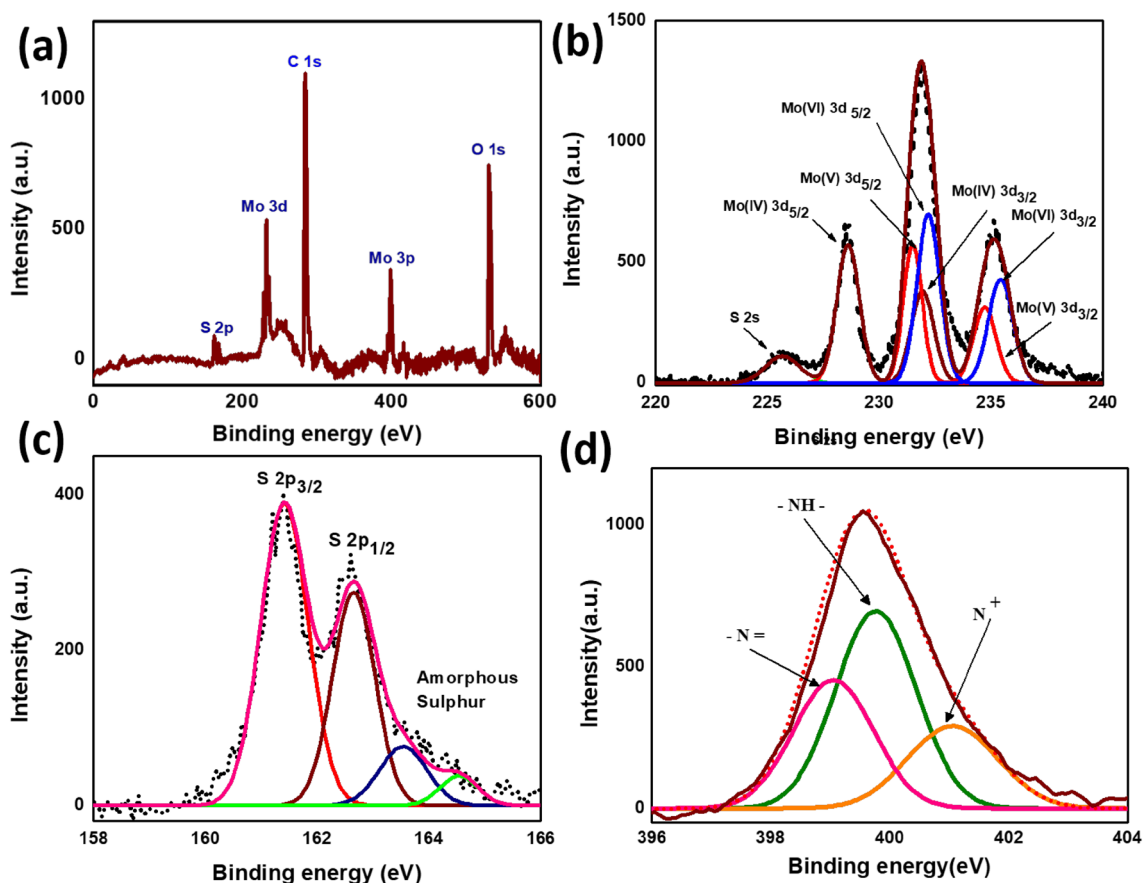
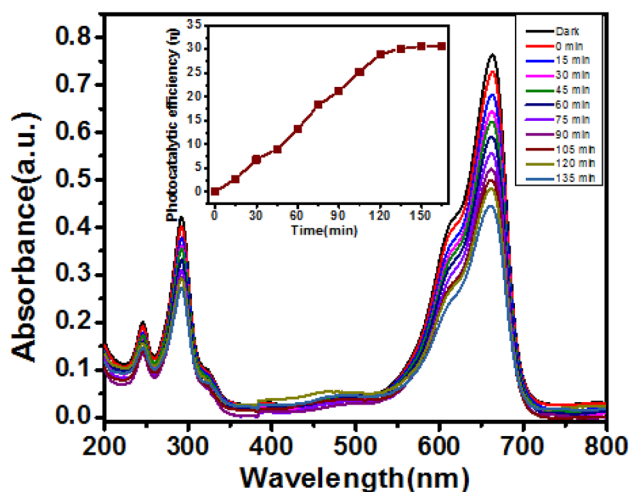**Fig. 8** XPS spectra **a** general scan, **b–d** deconvoluted core level scan of Mo (3d), S (2p) and N (1 s)

Fig. 9 Photocatalytic performance of MoS$_2$-PANI in the degradation of MB. Inset graph shows photocatalytic efficiency of MoS$_2$-PANI composite

Photocatalysis and analysis of intermediates of 4-CP degradation

Apart from the photocatalytic efficiency of MoS$_2$-PANI in the degradation of MB, the degradation of another common organic pollutant, 4-CP was also performed. The decrease in the concentration of 4-CP was indicated by its absorbance at 225 nm, as shown in Fig. 12.

MoS$_2$-PANI showed 75% efficiency in degrading 4-CP in 1 h. The intermediates formed during the degradation of 4-CP, when exposed to 45 min of UV radiation, are shown in Fig. 13. The intermediate found at a retention time of 5.7 min was due to the formation of benzoquinone. The other reaction intermediates observed at 8.6, 9.7, 11.7, 15 and 18.3 min are assigned to other intermediates mainly 4 Chlorocatechol and 4 Chlorophenol [36–39].

Photocatalytic mechanism

Figure 14 elucidates the processes of photoexcitation, charge separation and reaction in the MoS$_2$-PANI nanocomposite. The highest occupied molecular orbital
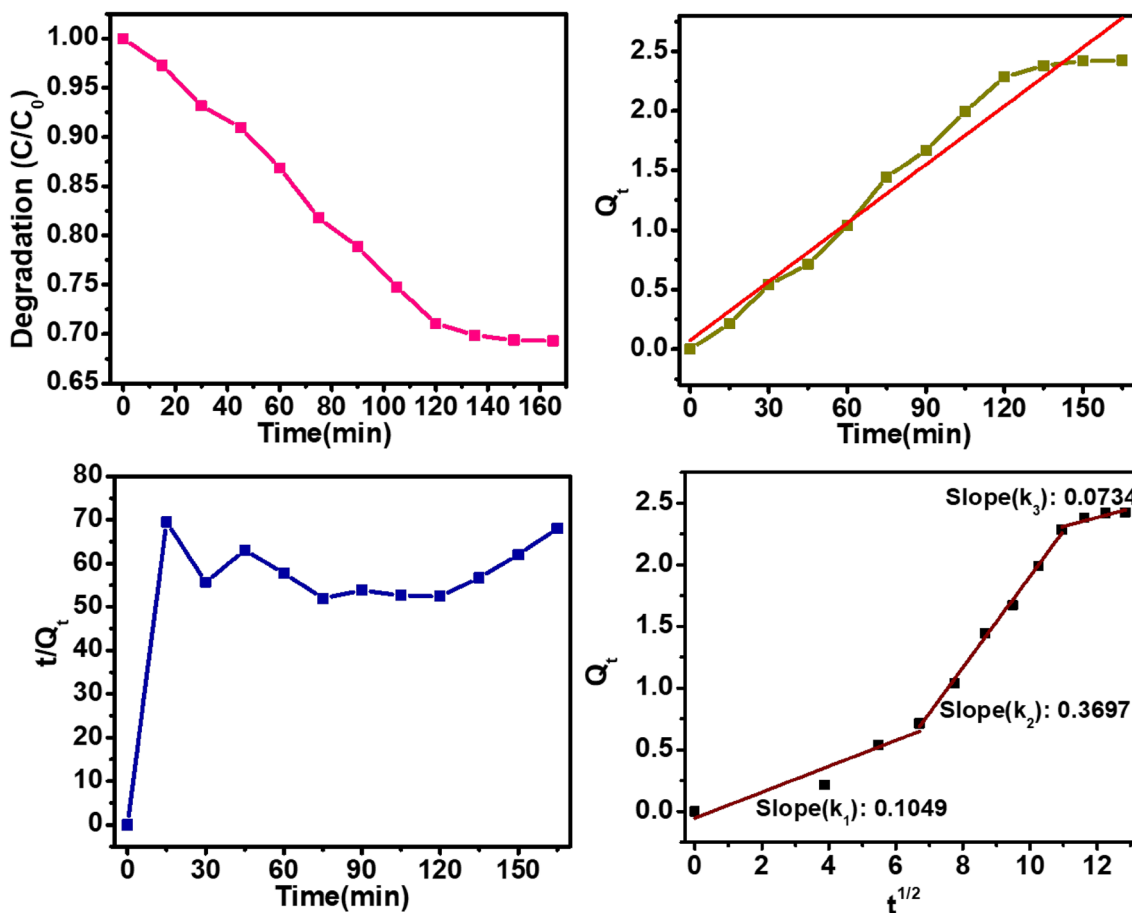
Fig. 10 **a** Photocatalytic degradation profile of MB, **b** pseudo first order kinetics model, **c** pseudo second order kinetics model, **d** intra particle diffusion model for MB on the surface of MoS_2-PANI composite

Table 1 The fitting results of all the models

First order model	
K_1 (g mg^{-1} min^{-1})	0.0163
Q_e (mg g^{-1})	0.0740
R^2	0.9623
Second order model	
K_2 (g mg^{-1} min^{-1})	0.1449
Q_e (mg g^{-1})	41.7091
R^2	0.1104
Intra-particle diffusion method	
K_1 (g mg^{-1} min^{-1})	0.1049
K_2 (g mg^{-1} min^{-1})	0.3697
K_3 (g mg^{-1} min^{-1})	0.0734

(HOMO) and the lowest unoccupied molecular orbital (LUMO) of PANI are 0.8 eV and − 1.9 eV respectively. The valence band (VB) and conduction band (CB) potentials of MoS_2 are 1.93 eV and − 0.07 eV, respectively. When irradiated with sunlight, induced PANI undergoes
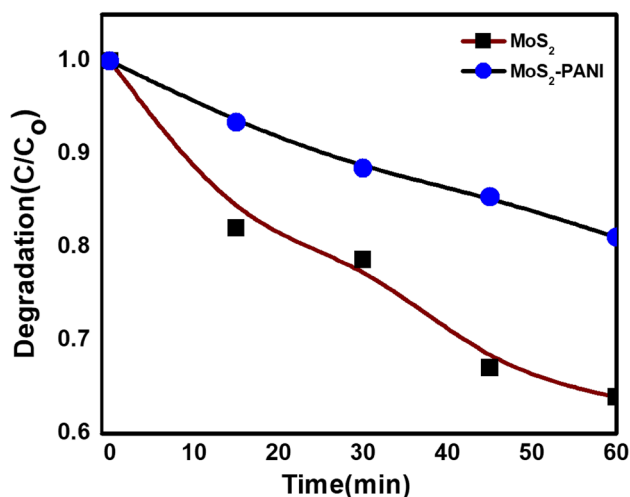

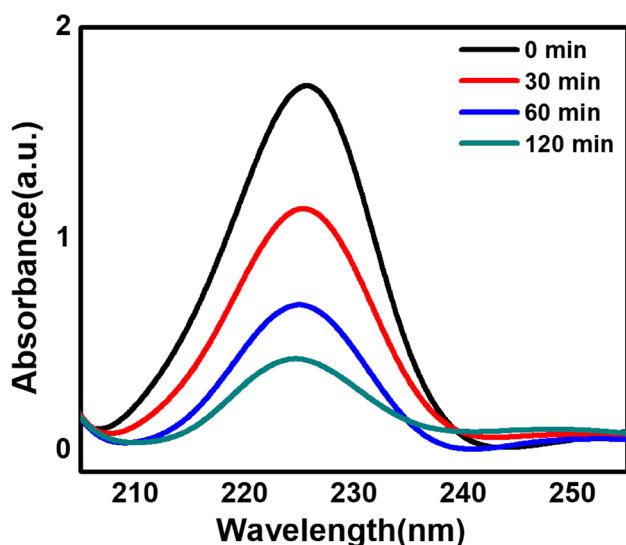**Fig. 11** Degradation profile for MoS_2 and MoS_2-PANI composite for MB degradation

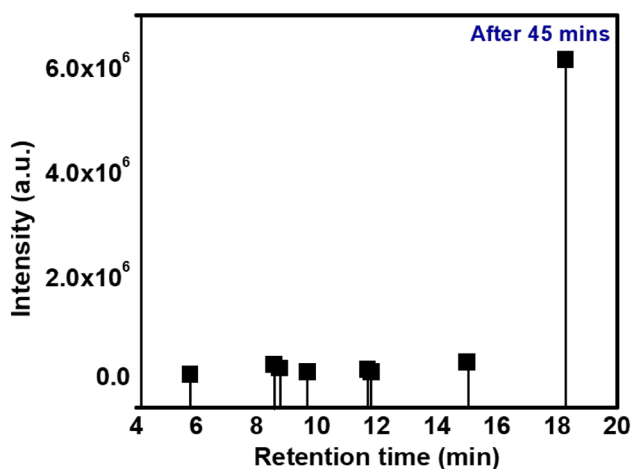**Fig. 12** Photocatalytic performance of MoS$_2$-PANI composite in degradation of 4-CP

Fig. 14 Mechanism for photocatalysis in MoS$_2$-PANI composite

oxygen radicals (O$_2^{\bullet}$, OH$^{\bullet}$) thus formed, act as oxidizers and help degrade organic pollutants. Electrons from CB of MoS$_2$ can also migrate to the LUMO of PANI, and thereby recombine with the holes of PANI, which are otherwise independently available for the generation of OH radical. Generated OH$^{\bullet}$ radicals are the most powerful reactive oxide species (ROS) which react with other OH$^{\bullet}$ radicals to form hydrogen peroxide (H$_2$O$_2$), which is another effective oxidizing agent for the degradation of organic dyes. Therefore, the synergistic effect between MoS$_2$ and PANI leads to photogenerated charge separation and reduced charge recombination which significantly enhances the photocatalytic activity of the MoS$_2$-PANI photocatalyst [13, 41, 42].

$$\text{MoS}_2\text{-PANI} + h\nu \rightarrow e^- + \text{h}^+\left(\text{MoS}^2\text{-PANI}\right): \\ \text{Generation of } e^- - h^+ \text{ pairs} \tag{4}$$

$$(e)^-\text{CB}_{\text{PANI}} \rightarrow (e)^-\text{CB}_{\text{MoS}_2} : \text{Transfer of } e^- \text{ from CB}_{\text{PANI}} \text{ to CB}_{\text{MoS}_2} \tag{5}$$

$$(e)^-\text{CB}_{\text{MoS}_2} + \text{O}_2 \rightarrow \text{O}_2^{\bullet-} : \text{Oxygen ionosorption} \tag{6}$$

$$\text{H}_2\text{O} \rightarrow \text{H}^+ + \text{OH}^- : \text{Ionization of water} \tag{7}$$

$$\text{O}_2^{\bullet-} + \text{H}^+ \rightarrow \text{HO}_2^{\bullet} : \text{Protonation of superoxides} \tag{8}$$

$$\text{HO}_2^{\bullet} + (e)^-\text{CB}_{\text{MoS}_2} \rightarrow \text{HO}_2^- \tag{9}$$

$$\text{HO}_2^- + \text{H}^+ \rightarrow \text{H}_2\text{O}_2 \tag{10}$$

Fig. 13 HPLC chromatogram for intermediates formed during 4-CP degradation

π–π* transition wherein the excited state electron is transported from the π to the π* orbital. The LUMO of PANI is at an energy level higher than that of MoS$_2$; these excited electrons are readily transferred to the CB of MoS$_2$ and eventually reach the surface of the catalyst to react with water and oxygen molecules and produce hydroxyl and superoxide radicals, which help to oxidize organic pollutants. Correspondingly, when MoS$_2$ absorbs sunlight, photo-excited electron–hole pairs are generated. The holes in the VB of MoS$_2$ can easily transfer to the HOMO of PANI. PANI being a good transporter of holes [40], enables the migration of the holes to the surface of the catalyst and can, therefore, oxidize the contaminants. The
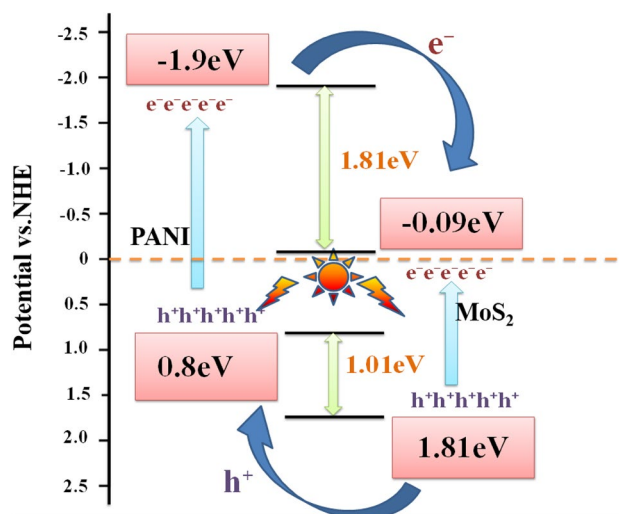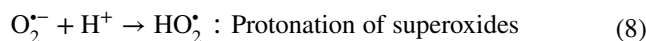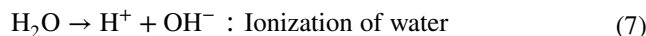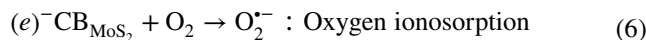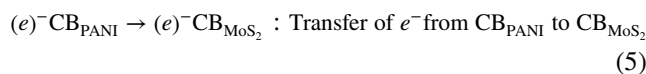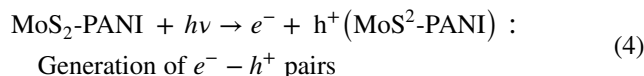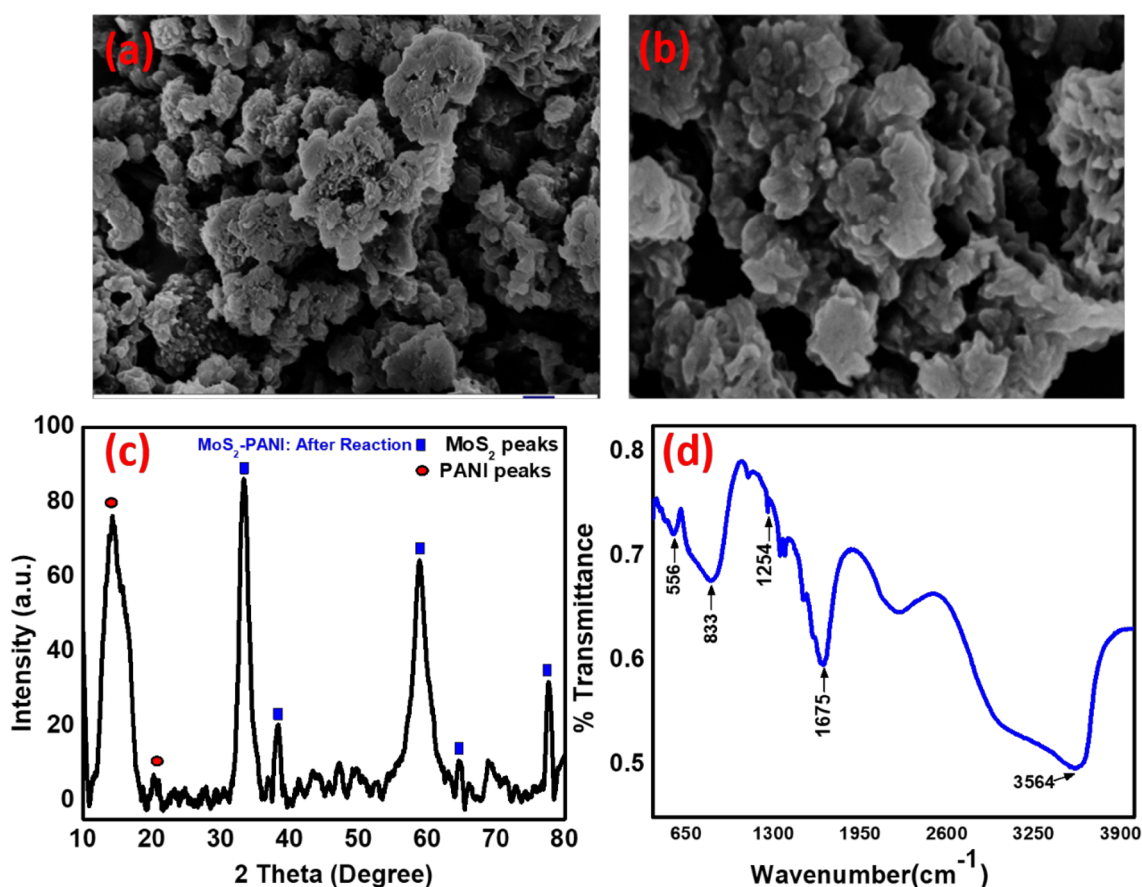
Fig. 15 **a**, **b** SEM images, **c** XRD peaks, **d** FTIR spectrum of MoS$_2$-PANI composite after reaction

Analysis of MoS$_2$-PANI after photocatalytic activity

Figure 15a, b shows the SEM images of the nanocomposite after it was used for the degradation of MB. The images indicate that the distinct PANI nanosheets clearly visible in MoS$_2$-PANI prior to the reaction are bundled up, post reaction. Figure 15c shows the XRD peaks for the nanocomposite after the reaction. It is evident from the peaks that the composition of the photocatalyst was not significantly affected after the reaction and this is further confirmed by the FTIR spectrum (Fig. 15d). The molecular structure of the nanocomposite after the reaction remained intact.

Conclusion

In this paper, we report the synthesis of a novel MoS$_2$-PANI nanocomposite through an in situ polymerization process. The sample was successfully characterised by SEM, TEM, XRD, FTIR, BET pore size analysis, XPS and UV–Vis spectroscopy techniques. The structural and morphological properties in addition to pore size and volume were also

determined. The oxidation states of different elements present in the sample, were confirmed by XPS. The photocatalytic efficiency of the synthesized nanocomposite, indicates that the composite favours dye adsorption and is found to be photocatalytically active, stable and capable of degradation of organic dyes. Kinetic investigations indicate that the photocatalytic reaction is driven by pseudo first order ($k_1 = 0.0163$ g mg^{-1} min^{-1} and $R^2 = 0.9623$ g mg^{-1} min^{-1}) adsorption model. The synergy between MoS$_2$ nanosheets and PANI may have an important role in improving photocatalytic efficiency and rate kinetics as a result of which, the synthesized MoS$_2$-PANI sample can act as a promising photocatalyst.

Compliance with ethical standards

Conflict of interest The authors declare no conflicts of interest.

References

1. Song, I., Park, C., Choi, H.C.: Synthesis and properties of molybdenum disulphide: from bulk to atomic layers. RSC Adv. **5**(10), 7495–7514 (2015). https://doi.org/10.1039/C4RA11852A

2. Chaudhary, N., Khanuja, M., Islam, S.: Hydrothermal synthesis of MoS$_2$ nanosheets for multiple wavelength optical sensing applications. Sens. Actuator A-Phys. **277**, 190–198 (2018). https://doi.org/10.1016/j.sna.2018.05.008

3. Singhal, C., Khanuja, M., Chaudhary, N., Pundir, C., Narang, J.: Detection of chikungunya virus DNA using two-dimensional MoS$_2$ nanosheets based disposable biosensor. Sci. Rep. **8**(1), 7734 (2018). https://doi.org/10.1038/s41598-018-25824-8

4. Li, J., Tang, W., Yang, H., Dong, Z., Huang, J., Li, S., Wang, J., Jin, J., Ma, J.: Enhanced-electrocatalytic activity of Ni$_{1-x}$Fe$_x$ alloy supported on polyethyleneimine functionalized MoS$_2$ nanosheets for hydrazine oxidation. RSC Adv. **4**(4), 1988–1995 (2014). https://doi.org/10.1039/C3RA42757A

5. Zeng, X., Niu, L., Song, L., Wang, X., Shi, X., Yan, J.: Effect of polymer addition on the structure and hydrogen evolution reaction property of nanoflower-like molybdenum disulfide. Metals **5**(4), 1829–1844 (2015). https://doi.org/10.3390/met5041829

6. Siddiqui, I., Mittal, H., Kohli, V.K., Gautam, P., Ali, M., Khanuja, M.: Hydrothermally synthesized micron sized, broom-shaped MoSe$_2$ nanostructures for superior photocatalytic water purification. Mater. Res. Express **5**(12), 125020 (2018). https://doi.org/10.1088/2053-1591/aae241

7. Ma, L., Chen, W.-X., Xu, Z.-D., Xia, J.-B., Li, X.: Carbon nanotubes coated with tubular MoS$_2$ layers prepared by hydrothermal reaction. Nanotechnology **17**(2), 571 (2006). https://doi.org/10.1088/0957-4484/17/2/038

8. Huang, G., Chen, T., Chen, W., Wang, Z., Chang, K., Ma, L., Huang, F., Chen, D., Lee, J.Y.: Graphene-like MoS2/graphene composites: cationic surfactant-assisted hydrothermal synthesis and electrochemical reversible storage of lithium. Small **9**(21), 3693–3703 (2013). https://doi.org/10.1002/smll.201300415

9. Singh, S., Sharma, R., Khanuja, M.: A review and recent developments on strategies to improve the photocatalytic elimination of organic dye pollutants by BiOX (X = Cl, Br, I, F) nanostructures. Korean J. Chem. Eng. **35**, 1955 (2018). https://doi.org/10.1007/s11814-018-0112-y

10. Singh, S., Ruhela, A., Rani, S., Khanuja, M., Sharma, R.: Concentration specific and tunable photoresponse of bismuth vanadate functionalized hexagonal ZnO nanocrystals based photoanodes for photoelectrochemical application. Solid State Sci. **76**, 48–56 (2018). https://doi.org/10.1016/j.solidstatesciences.2017.12.003

11. Boeva, Z.A., Sergeyev, V.: Polyaniline: synthesis, properties, and application. Polym. Sci. Ser. C **56**(1), 144–153 (2014). https://doi.org/10.1134/S1811238214010032

12. Sharma, R., Khanuja, M., Islam, S., Singhal, U., Varma, A.: Aspect-ratio-dependent photoinduced antimicrobial and photocatalytic organic pollutant degradation efficiency of ZnO nanorods. Res. Chem. Intermed. **43**(10), 5345–5364 (2017). https://doi.org/10.1007/s11164-017-2930-7

13. Deng, Y., Tang, L., Zeng, G., Dong, H., Yan, M., Wang, J., Hu, W., Wang, J., Zhou, Y., Tang, J.: Enhanced visible light photocatalytic performance of polyaniline modified mesoporous single crystal TiO$_2$ microsphere. Appl. Surf. Sci. **387**, 882–893 (2016). https://doi.org/10.1016/j.apsusc.2016.07.026

14. Zhang, N., Ma, W., Wu, T., Wang, H., Han, D., Niu, L.: Edge-rich MoS$_2$ naonosheets rooting into polyaniline nanofibers as effective catalyst for electrochemical hydrogen evolution. Electrochim. Acta **180**, 155–163 (2015). https://doi.org/10.1016/j.electacta.2015.08.108

15. Ren, L., Zhang, G., Yan, Z., Kang, L., Xu, H., Shi, F., Lei, Z., Liu, Z.-H.: Three-dimensional tubular MoS$_2$/PANI hybrid electrode for high rate performance supercapacitor. ACS Appl. Mater. Interfaces. **7**(51), 28294–28302 (2015). https://doi.org/10.1021/acsami.5b08474

16. Chang, K.C., Hsu, C.H., Peng, C.W., Huang, Y.Y., Yeh, J.M., Wan, H.P., Hung, W.C.: Preparation and comparative properties of membranes based on PANI and three inorganic fillers. Express Polym. Lett. **8**(3), 207–218 (2014). https://doi.org/10.3144/expresspolymlett.2014.24

17. Popa, A., Plesu, N., Sasca, V., Kis, E.E., Marinkovic-Neducin, R.: Physicochemical features of polyaniline supported heteropolyacids. J. Optoelectron. Adv. Mater. **8**(5), 1944–1950 (2006)

18. Kondawar, S., Deshpande, M., Agrawal, S.: Transport properties of conductive polyaniline nanocomposites based on carbon nanotubes. Int. J. Compos. Mater. **2**(3), 32–36 (2015). https://doi.org/10.5923/j.cmaterials.20120203.03

19. Haldorai, Y., Shim, J.-J.: Synthesis of polyaniline/Q-CdSe composite via ultrasonically assisted dynamic inverse emulsion polymerization. Colloid Polym. Sci. **289**(7), 849–854 (2011). https://doi.org/10.1007/s00396-011-2400-5

20. Gao, Y., Chen, C., Tan, X., Xu, H., Zhu, K.: Polyaniline-modified 3D-flower-like molybdenum disulfide composite for efficient adsorption/photocatalytic reduction of Cr(VI). J. Colloid Interface Sci. **476**, 62–70 (2016). https://doi.org/10.1016/j.jcis.2016.05.022

21. Yuwen, L., Xu, F., Xue, B., Luo, Z., Zhang, Q., Bao, B., Su, S., Weng, L., Huang, W., Wang, L.: General synthesis of noble metal (Au, Ag, Pd, Pt) nanocrystal modified MoS$_2$ nanosheets and the enhanced catalytic activity of Pd–MoS$_2$ for methanol oxidation. Nanoscale **6**(11), 5762–5769 (2014). https://doi.org/10.1039/c3nr06084e

22. Patil, P.T., Anwane, R.S., Kondawar, S.B.: Development of electrospun polyaniline/ZnO composite nanofibers for LPG sensing. Procedia Mater. Sci. **10**, 195–204 (2015). https://doi.org/10.1016/j.mspro.2015.06.041

23. Hu, F., Li, W., Zhang, J., Meng, W.: Effect of graphene oxide as a dopant on the electrochemical performance of graphene oxide/polyaniline composite. J. Mater. Res. Technol. **30**(4), 321–327 (2014). https://doi.org/10.1016/j.jmst.2013.10.009

24. Gogoi, G., Arora, S., Vinothkumar, N., De, M., Qureshi, M.: Quaternary semiconductor Cu$_2$ZnSnS$_4$ loaded with MoS$_2$ as a co-catalyst for enhanced photo-catalytic activity. RSC Adv. **5**(51), 40475–40483 (2015). https://doi.org/10.1039/C5RA03401A

25. Hu, L., Ren, Y., Yang, H., Xu, Q.: Fabrication of 3D hierarchical MoS$_2$/polyaniline and MoS$_2$/C architectures for lithium-ion battery applications. ACS Appl. Mater. Interfaces. **6**(16), 14644–14652 (2014). https://doi.org/10.1021/am503995s

26. Khanuja, M., Mehta, B.R., Shivaprasad, S.M.: J. Chem. Sci. **120**, 573–578 (2008). https://doi.org/10.1007/s12039-008-0087-z

27. Khanuja, M., Kala, S., Mehta, B.R., Sharma, H., Shivaprasad, S.M., Balamurgan, B., Kruis, F.E.: XPS and AFM studies of monodispersed Pb/PbO core–shell nanostructures. J. Nanosci. Nanotechnol. **7**(6), 2096–2100 (2007). https://doi.org/10.1166/jnn.2007.776

28. Binkauskienė, E., Jasulaitienė, V., Lugauskas, A.: Effect of Aspergillus niger Tiegh L-10 on the physical and chemical properties of a polyaniline coating in the growth substrate. Synth.

Met. **159**(13), 1365–1368 (2009). https://doi.org/10.1016/j.synthmet.2009.03.011

29. Huang, Q., Liu, M., Chen, J., Wan, Q., Tian, J., Huang, L., Jiang, R., Wen, Y., Zhang, X., Wei, Y.: Facile preparation of MoS_2 based polymer composites via mussel inspired chemistry and their high efficiency for removal of organic dyes. Appl. Surf. Sci. **419**, 35–44 (2017). https://doi.org/10.1016/j.apsusc.2017.05.006

30. Massey, A.T., Gusain, R., Kumari, S., Khatri, O.P.: Hierarchical microspheres of MoS_2 nanosheets: efficient and regenerative adsorbent for removal of water-soluble dyes. Ind. Eng. Chem. Res. **55**(26), 7124–7131 (2016). https://doi.org/10.1021/acs.iecr.6b01115

31. Han, S., Liu, K., Hu, L., Teng, F., Yu, P., Zhu, Y.J.S.R.: Superior adsorption and regenerable dye adsorbent based on flower-like molybdenum disulfide nanostructure. Sci Rep. **7**, 43599 (2017). https://doi.org/10.1038/srep43599

32. Ashraf, W., Fatima, T., Srivastava, K., Khanuja, M.: Superior photocatalytic activity of tungsten disulfide nanostructures: role of morphology and defects. Appl. Nanosci. (2019). https://doi.org/10.1007/s13204-019-00951-4

33. Takijiri, K., Morita, K., Nakazono, T., Sakai, K., Ozawa, H.: Highly stable chemisorption of dyes with pyridyl anchors over TiO_2: application in dye-sensitized photoelectrochemical water reduction in aqueous media. Chem. Commun. **53**(21), 3042–3045 (2017). https://doi.org/10.1039/C6CC10321A

34. Qiao, X.Q., Hu, F.C., Tian, F.Y., Hou, D.F., Li, D.S.: Equilibrium and kinetic studies on MB adsorption by ultrathin 2D MoS_2 nanosheets. Rsc Adv. **6**(14), 11631–11636 (2016). https://doi.org/10.1039/C5RA24328A

35. Li, J., Hou, Y., Gao, X., Guan, D., Xie, Y., Chen, J., Yuan, C.: A three-dimensionally interconnected carbon nanotube/layered MoS2 nanohybrid network for lithium ion battery anode with superior rate capacity and long-cycle-life. Nano Energy **16**, 10–18 (2015). https://doi.org/10.1016/j.nanoen.2015.05.025

36. Li, X., Cubbage, J.W., Jenks, W.S.: Photocatalytic degradation of 4-chlorophenol. 2. The 4-chlorocatechol pathway. J. Org. Chem. **64**(23), 8525–8536 (1999). https://doi.org/10.1021/jo990912n

37. Nguyen, A.T., Juang, R.-S.: Photocatalytic degradation of p-chlorophenol by hybrid H_2O_2 and TiO_2 in aqueous suspensions under UV irradiation. J. Environ. Manag. **147**, 271–277 (2015)

38. Bian, W., Song, X., Liu, D., Zhang, J., Chen, X.: The intermediate products in the degradation of 4-chlorophenol by pulsed high voltage discharge in water. J. Hazard. Mater. **192**(3), 1330–1339 (2011). https://doi.org/10.1016/j.jhazmat.2011.06.045

39. Al-Sayyed, G., D'Oliveira, J.-C., Pichat, P.: Semiconductor-sensitized photodegradation of 4-chlorophenol in water. J. Photochem. Photobiol. A Chem. **58**(1), 99–114 (1991). https://doi.org/10.1016/1010-6030(91)87101-Z

40. Tan, S., Zhai, J., Wan, M., Meng, Q., Li, Y., Jiang, L., Zhu, D.: Influence of small molecules in conducting polyaniline on the photovoltaic properties of solid-state dye-sensitized solar cells. J. Phys. Chem. B **108**(48), 18693–18697 (2004). https://doi.org/10.1021/jp046574y

41. Ameen, S., Akhtar, M.S., Kim, Y.S., Yang, O.-B., Shin, H.-S.: An effective nanocomposite of polyaniline and ZnO: preparation, characterizations, and its photocatalytic activity. Colloid Polym. Sci. **289**(4), 415–421 (2011). https://doi.org/10.11113/mjfas.v0n0.562

42. Zhang, H., Zong, R., Zhao, J., Zhu, Y.: Dramatic visible photocatalytic degradation performances due to synergetic effect of TiO_2 with PANI. Environ. Sci. Technol. **42**(10), 3803–3807 (2008). https://doi.org/10.1021/es703037x